JCI insight

TECHNICAL ADVANCE

Two-photon imaging of the mammalian retina with ultrafast pulsing laser

Grazyna Palczewska,[1] Patrycjusz Stremplewski,[2] Susie Suh,[3] Nathan Alexander,[3] David Salom,[3] Zhiqian Dong,[1] Daniel Ruminski,[3] Elliot H. Choi,[3] Avery E. Sears,[3] Timothy S. Kern,[3] Maciej Wojtkowski,[2] and Krzysztof Palczewski[3]

[1]Polgenix, Inc., Department of Medical Devices, Cleveland, Ohio, USA. [2]Department of Physical Chemistry of Biological Systems, Institute of Physical Chemistry, Polish Academy of Sciences, Warsaw, Poland. [3]Department of Pharmacology, School of Medicine, Case Western Reserve University, Cleveland, Ohio, USA.

Noninvasive imaging of visual system components in vivo is critical for understanding the causal mechanisms of retinal diseases and for developing therapies for their treatment. However, ultraviolet light needed to excite endogenous fluorophores that participate in metabolic processes of the retina is highly attenuated by the anterior segment of the human eye. In contrast, 2-photon excitation fluorescence imaging with pulsed infrared light overcomes this obstacle. Reducing retinal exposure to laser radiation remains a major barrier in advancing this technology to studies in humans. To increase fluorescence intensity and reduce the requisite laser power, we modulated ultrashort laser pulses with high-order dispersion compensation and applied sensorless adaptive optics and custom image recovery software and observed an over 300% increase in fluorescence of endogenous retinal fluorophores when laser pulses were shortened from 75 fs to 20 fs. No functional or structural changes to the retina were detected after exposure to 2-photon excitation imaging light with 20-fs pulses. Moreover, wide bandwidth associated with short pulses enables excitation of multiple fluorophores with different absorption spectra and thus can provide information about their relative changes and intracellular distribution. These data constitute a substantial advancement for safe 2-photon fluorescence imaging of the human eye.

Introduction

Noninvasive assessment of physiological processes needed to sustain vision in humans is essential for detecting the earliest signs of progressive eye diseases, developing new therapeutics, and evaluating their efficacy. Typically, assessment of retinal health is accomplished through electrophysiological recordings and psychophysical tests in conjunction with fundus photography, scanning laser ophthalmoscopy (SLO), or optical coherence tomography (OCT) imaging (1–6). These techniques are well suited to measure the extent of retinal damage, though degeneration must be severe enough to reliably detect changes in the retina (7). Recently, OCT was applied to measure changes in the optical path through photoreceptor outer segments after visual stimulation (8, 9). However, available methodologies remain inadequate for detecting deviations at the cellular level in the retina that lead to degeneration. In addition, early evaluation of retinal health is critical for developing innovative treatments that preserve sight. To effect the management and outcome of currently incurable blinding diseases caused by genetic alternations, aging, or environmental insults, a new methodology is needed to visualize the retina safely at subcellular resolution and to assess the efficacy of pharmacological agents, grafted progenitor cells, and gene replacement.

Fortunately, the retina of the intact eye is generally accessible to optical methodology. Moreover, retinoid fluorophores that sustain vision provide an opportunity to investigate biochemical events related to retinal health (10). Over the last 2 decades, progress towards understanding the chemistry and biology of vision at the molecular level has been substantial (11–15). Activation of visual pigments in rod and cone photoreceptor cells is initiated by photoisomerization of the visual chromophore, 11-*cis*-retinylidene, to its all-*trans* configuration (10, 16). Regeneration of this 11-*cis* isomer, a derivative of vitamin A that is needed to maintain vision, occurs through a multistep process known as the retinoid visual cycle, located in photoreceptors, the retinal pigment epithelium (RPE), and possibly Müller cells (17). Additionally, byproducts of the retinoid visual cycle including *N*-retinylidene-*N*-retinylethanolamine (A2E) and other

Authorship note: GP and PS contributed equally to this work.

Conflict of interest: KP is Chief Scientific Officer at Polgenix, Inc. KP is also an inventor of the U.S. patent no. 7,706,863 and U.S. patent no. 8,346,345, whose values may be affected by this publication. GP and ZD are employees of Polgenix, Inc.

Submitted: April 9, 2018
Accepted: July 24, 2018
Published: September 6, 2018

Reference information:
JCI Insight. 2018;3(17): e121555.
https://doi.org/10.1172/jci.insight.121555.

retinal condensation products, are components of lipofuscin, which accumulates in the RPE with age and overaccumulates in disease states (18). Defects in various steps of the retinoid visual cycle have been linked to blinding diseases (17), and measuring its byproducts can provide an early indication of retinal health as well as a means to assess different therapies.

Two-photon excitation (TPE) fluorescence (TPEF) imaging of the eye with infrared (IR) light provides an opportunity for monitoring the retinoid visual cycle in subcellular detail. Because light scattering decreases at longer wavelengths, the IR light beam is less impacted by inhomogeneities of the ocular tissue; thus, it can maintain its shape throughout the approximately 250-μm thickness of the retina, in contrast to visible light. For retinal tissue, the photon transport mean free path at 400 nm can be estimated to be less than 40% of that at 780 nm (19). Moreover, 2-photon absorption is proportional to the square of the excitation light intensity (20), and 2-photon absorption cross sections are very small, on the order of 10^{-52} $cm^4 \cdot s$ per photon. Therefore, TPE occurs only around the focal volume, thus minimizing out-of-focus noise (21). Furthermore, the direct transmission through the anterior segment of the human eye is relatively low for wavelengths shorter than 400 nm, but it increases substantially for light wavelengths used in TPEF (22). Because fluorophores participating in the retinoid visual cycle have maximal absorptions at less than 400 nm when excited with a traditional 1-photon process (23), TPEF with IR light has the further potential for safely imaging and measuring changes in retinoids to assess retinal health in humans.

Equations indicating that the efficiency of generating TPEF is inversely proportional to the pulse duration and pulse repetition frequency (PRF) were derived in the 1990s (20); however, a reduced laser pulse duration is associated with an increased spectral bandwidth and concomitant dispersion and phase distortions introduced by the tissue and optical components of the imaging system, and previous efforts based on reducing PRF did not succeed in achieving scanning speeds, image size, or laser power levels appropriate for noninvasive imaging of the retina. Positive dispersion results in longer wavelengths arriving faster than shorter wavelengths, thus stretching laser pulses in the time domain at the imaged sample. Typically, a short laser pulse duration at the sample can be restored by introducing negative dispersion or dispersion pre-compensation, through incorporating a prism pair or a grating pair (24). For very short pulses, however, higher order dispersion terms (higher than second-order group delay dispersion or GDD) become significant, such that these precompensation methods often render unsatisfactory results, especially when applied in a complex microscope setup. Thus, more advanced dispersion compensation methods are required.

Performing noninvasive imaging of unstained tissue also is impacted by low quantum yields and absorbance spectra of endogenous fluorophores, light scattering, and wave-front distortion caused by the tissue layers between the tissue of interest and the objective, and limited-access window or numerical aperture (NA), which in the human eye is equal to 0.2. Subcellular images of endogenous retinoids in the retina have been obtained in mice and primates (25, 26). However, to achieve safe imaging in humans, laser light sufficient for visualizing cellular and biochemical components must be reduced. Significant progress has been made toward this goal by (a) improving the excitation beam focus by incorporating adaptive optics, and (b) registering and averaging low signal-to-noise TPEF images obtained with low laser power (27–33). TPEF also is inversely proportional to the pulse duration of the excitation light; thus, a laser delivering shorter pulses could have a major impact on lowering the laser energy required for imaging (20). TPEF imaging of the retina in vivo has not yet been achieved with laser pulses shorter than 45 fs. Side-by-side comparisons of TPE efficiency of endogenous fluorophores with different laser pulse durations and bandwidths in the fs range also are lacking, even for in vitro systems.

Here, we compared 75-fs, 32-fs, and 20-fs laser pulses for imaging areas of retina larger than 1 × 1 mm in mice with well-defined genetic defects that cause degenerative retinal diseases in humans. The duration of short laser pulses was preserved at the sample plane by using a custom spatial light modulator (SLM) and a diffraction grating–based dispersion compensation system. The mean fluorescence from the RPE of mouse models of human retinal pathology probed with 20-fs laser pulses was approximately 3 times greater than that measured with 75-fs laser pulses with the same average power and center wavelength. Moreover, using a diverse set of structural, functional, and biochemical measurements we did not detect any changes to the structure nor functionality of retina after TPEF imaging. The findings reported here reveal important progress towards safe TPEF imaging of fundamental biochemical events contributing to vision and health of the human eye.

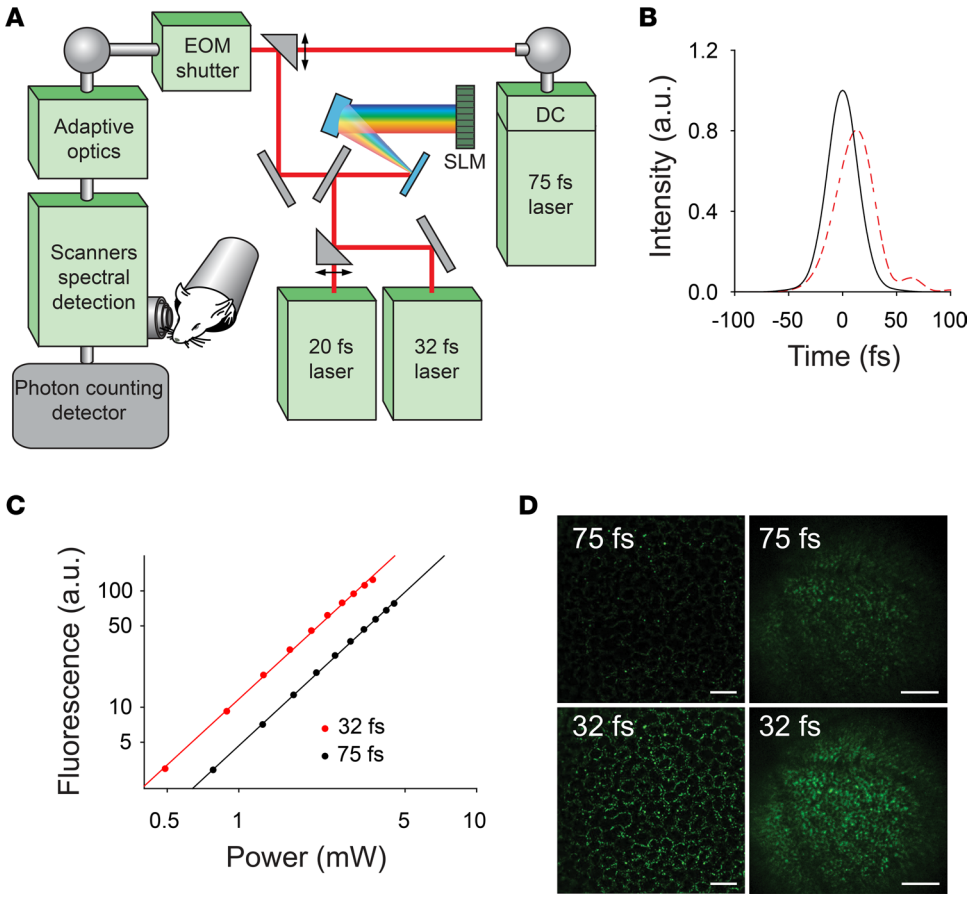

Figure 1. Noninvasive TPEF imaging of mouse retina. (**A**) Depiction of the experimental setup that includes a dispersion compensation system, adaptive optics, an electro-optic modulator (EOM) and 3 lasers: (i) a tunable-wavelength and -pulse-duration laser capable of delivering 20-fs pulses; (ii) a laser with a fixed pulse duration at 75 fs and a tunable wavelength, and (iii) a laser with a fixed pulse duration at 32 fs and fixed wavelength at 740 nm. Two black, dual arrowheads indicate switching locations between the lasers. The 75-fs laser is equipped with a prism pair–based dispersion compensation unit (DC). Light beams from 20-fs and 32-fs lasers are routed through a diffraction grating and spatial light modulator–based (SLM-based), custom-built diffraction compensation system. (**B**) Calculated temporal profiles of 32-fs Gaussian-shaped pulses: black represents bandwidth limited, and red represents pulse impacted by third-order dispersion (calculated for the amount of NBK7 glass generating a GDD equivalent to that of the optical setup). (**C**) Mean TPEF from a paper target, as a function of excitation power, acquired with 75-fs and 32-fs lasers. Solid circles represent measured data points; solid lines represent the linear data fit with slopes equal to 1.9. (**D**) TPEF images of mouse RPE obtained with 740-nm excitation with both 75-fs and 32-fs pulses after optimization of dispersion compensation. Ex vivo (left column) and in vivo (right column); images of the RPE obtained with 75-fs laser in the upper row, images obtained with 32-fs laser are shown in the bottom row. Ex vivo images were obtained with 6.3 mW, in vivo images were obtained with 7.5 mW; image acquisition time was 2.6 seconds. Ratios of mean pixel gray value of TPEF images of the RPE in *Rpe65*$^{-/-}$ mice obtained with a 32-fs laser to that obtained with a 75-fs laser were equal to 2.9 ex vivo and 2.2 in vivo. Scale bars: 50 μm ex vivo (left column); 200 μm in vivo (right column).

Results

To obtain images of retinoid visual cycle components within the retinas of living animals using low laser power, several critical factors required both innovation and optimization. To minimize pulse duration at the sample, high-order dispersion compensation was integrated with the laser delivering pulses as short as 20 fs. Sensorless adaptive optics were incorporated to improve spatial focusing of the laser beam. Postprocessing of the data included registration and averaging of single-frame images to further reduce laser light exposure needed to obtain informative images.

Configuration of the dispersion compensation system. GDD introduced by the microscope arrangement without dispersion compensation was estimated to be 27,000 fs^2. This estimate was determined by measuring an autocorrelation function (ACF) at the objective focal plane and at the entry to the electro-optic modulator (EOM) (Figure 1A). A dispersion compensation unit integrated with the Vision S laser sufficed

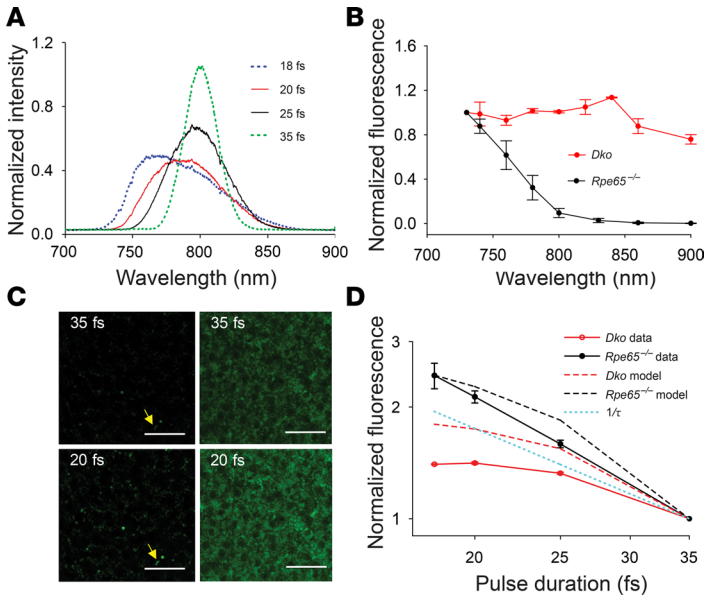

Figure 2. Impact of pulse duration on TPEF of native retinal fluorophores. (**A**) Spectra of laser light with different pulse durations as measured in the sample plane. (**B**) Two-photon excitation spectra from the RPE of *Abca4*$^{-/-}$ *Rdh8*$^{-/-}$ (*Dko*) and *Rpe65*$^{-/-}$ mice. Plotted are mean gray pixel values from areas equivalent to at least 10 RPE cells. (**C**) Images of RPE in *Rpe65*$^{-/-}$ (left panels) and in *Dko* (right panels) mice. Durations of laser pulses are indicated in each image. Small green-colored dots indicated with yellow arrows are retinosomes. To avoid saturation of the detector when imaging retinosomes, both the gain and laser power were kept low. Thus, retinosomes are only faintly visible in images obtained with 35-fs light as compared with images obtained with 20-fs light. Scale bars: 50 μm. Images of *Rpe65*$^{-/-}$ were obtained with 5.5 mW, and images of *Dko* were obtained with 4.9 mW, and image acquisition time was 2.6 seconds. (**D**) RPE fluorescence measured as mean gray pixel values of the raw images obtained with laser light pulses at 18 fs, 20 fs, 25 fs, and 35 fs durations. Data were analyzed as mean gray pixel values from areas equivalent to at least 10 RPE cells. Solid, filled symbols represent measured data points, dashed lines represent results of modeling. Dotted cyan line represents fit to 1/pulse duration (1/τ). Data are shown as means ± SD, n = 3.

for 75-fs pulses (as confirmed by measuring a 70-fs pulse duration at the sample plane with an autocorrelator), but a more elaborate scheme was required for ultrashort pulses. The first attempt to compensate for the dispersion associated with short laser pulses involved the use of a chirped mirror–based dispersion compensator (Supplemental Figure 1A; supplemental material available online with this article; https://doi.org/10.1172/jci.insight.121555DS1). Tuning the amount of negative dispersion was achieved by changing the number of laser light bounces between pairs of chirped mirrors, and monitoring ACF at the sample plane (34). Each bounce introduced a negative GDD of approximately 700 fs^2. Contrary to expectation, the TPEF signal obtained with this dispersion compensation and a 32-fs laser was nearly the same as that obtained with a 75-fs laser, possibly reflecting the presence of high-order dispersion terms, especially third-order dispersion (TOD). To confirm the impact of TOD on pulse distortions, a numerical simulation of the pulse temporal profile was performed in the presence of TOD only (see supplemental methods). In this calculation, the GDD was assumed perfectly precompensated and that pulse broadening was a result of TOD (no impact of chirped mirrors on TOD was assumed). The 32-fs pulse impacted by TOD had a reduced peak power and was elongated in the time domain as compared with a 32-fs Gaussian transform–limited pulse (Figure 1B), consistent with the reduction in TPEF. Moreover, the presence of TOD was visible in the envelope of the ACF as side-lobes around the central peak (Supplemental Figure 1B). Thus, even perfect compensation of GDD was insufficient for a 32-fs laser with full width, half maximum (FWHM) spectral bandwidths larger than approximately 20 nm, as the higher order dispersion terms introduced a substantial phase distortion. Therefore, to compensate for higher order dispersion terms, a customized diffraction grating and spatial light modulator–based (SLM-based) multiphoton intrapulse interference phase system (MIIPS) (35) were introduced. The MIIPS operation required collection of second harmonic (SH) signals from the nonlinear crystal placed at the focal plane of the microscope objective, while spectral components of the pulse were phase shifted by the SLM. Thus, the phases of the spectral components of the pulse were iteratively adjusted to cancel out the phase shifts introduced by dispersive media. Optimal configurations

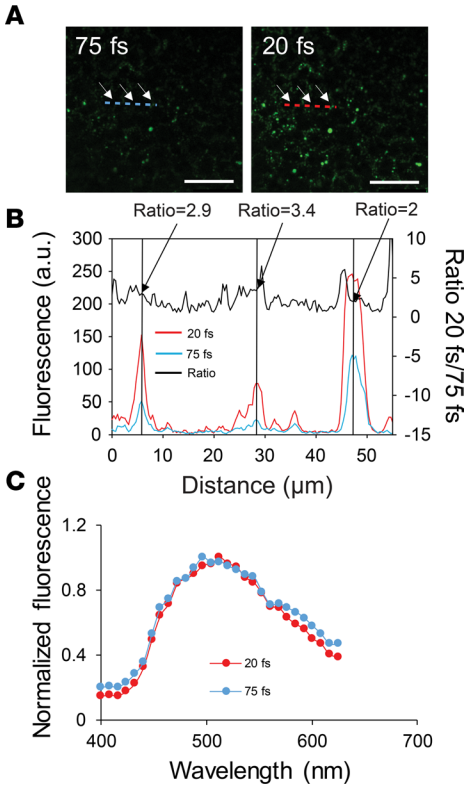

Figure 3. Increase in TPEF from the RPE of 2-month-old *Rpe65*$^{-/-}$ mice illuminated with 20-fs pulsed light. (**A**) Representative images of the RPE in the intact ex vivo mouse eye. Laser pulse durations are indicated in each image. White arrows point to retinosomes. Dashed lines outline the locations where fluorescence intensity profiles were measured. Scale bars: 50 μm. Images were obtained in 2.6 seconds with 6.2 mW. (**B**) TPEF intensity profiles from locations along the dashed lines shown in **A**. Measured fluorescence is plotted on the left vertical axis and the ratio of the fluorescence excited with 20-fs light to that excited with 75-fs light is plotted on the right vertical axis. Black arrows indicate data for retinosomes along the TPEF fluorescence profiles. (**C**) Fluorescence emission spectra in response to 790-nm 20-fs and 75-fs light.

of the SLM (so-called masks) were measured for each objective and the required laser wavelengths. These masks then were used for measurements of ACF and after replacing the SH crystal with a sample for imaging. The FWHM pulse duration was 33 fs for the 32-fs laser, and 21 fs for the 20-fs laser (Supplemental Figure 2); moreover, no side-lobes were detected in the ACF. Thus, it was confirmed that using a custom MIIPS preserved the duration of short laser pulses at the sample plane.

The impact of reducing pulse duration on TPEF was first evaluated using a paper target that absorbs 745-nm light through 2-photon absorption, and then emits visible light (Figure 1C). A series of TPEF images was obtained from the same region of the sample by employing both 32- and 75-fs lasers with variable laser powers. The linear fit through the data had a slope of 1.9 on a log-log plot, confirming TPE by both lasers. The mean gray pixel value used as a measure of TPEF was 2.8 times higher for images obtained with a 32-fs laser pulse compared with those obtained with a 75-fs pulse. The increase in TPEF measured for the same laser power was then determined in *Rpe65*$^{-/-}$ mice. Mean fluorescence from the RPE of those mice probed with 32-fs laser pulses was 2.9 times greater than that from 75-fs laser pulses measured ex vivo, and 2.2 times greater when measured in vivo with the same average power and center wavelength (Figure 1D).

Impact of the bandwidth of ultrashort laser pulses on TPEF of native retinal fluorophores. Considering the positive results obtained with the fixed-pulse-duration 32-fs laser and the uncertainty about the potential of very short, wide-bandwidth pulses on improving the efficiency and quality of TPEF imaging of endogenous fluorophores, a laser with an adjustable bandwidth and pulse duration (identified as 20 fs in Figure 1A) was incorporated into the microscope system. Not every combination of pulse bandwidth and center wavelength within the tuning range was achievable. Spectra of 18-, 20-, 25-, and 35-fs pulses were measured at the sample plane (Figure 2A), and FWHM spectral bandwidths of these pulses were 70, 65, 50, and 28 nm, respectively. The λ_{max} was not the same for these pulses; the 18-fs pulse had a broad maximum around 768 nm, the 20-fs pulse had a broad maximum around 790 nm, the 25-fs pulse at 796 nm, and the 35-fs pulse at 799 nm. The average laser power delivered to the sample for each of these conditions was the same.

Excitation spectra from the RPE were then measured in 2 mouse models of retinal pathology with a 75-fs tunable laser (Figure 2B). TPE spectra were measured in *Rpe65*$^{-/-}$ mice. The spectra showed a relatively monotonic decline of the fluorescence signal for excitation wavelengths longer than 730 nm, and almost no fluorescence for wavelengths longer than 800 nm. In contrast, fluorescence from *Abca4*$^{-/-}$ *Rdh8*$^{-/-}$ (*Dko*) mice varied within 20% from 730 nm to 840 nm and had a maximum at 840 nm. Images of *Dko* and *Rpe65*$^{-/-}$ mouse retinas obtained with the same laser power reveal an increased fluorescence in images

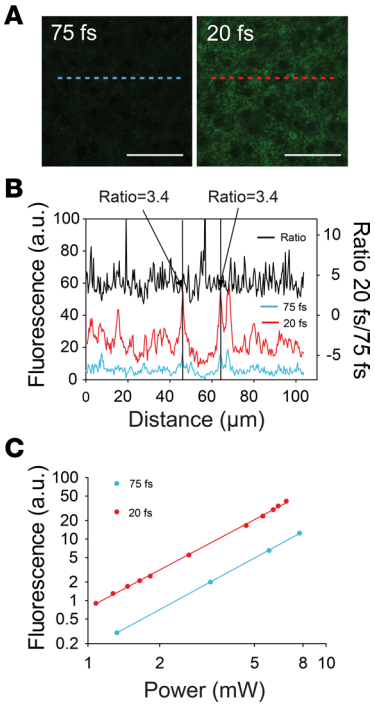

Figure 4. Increase in TPEF from the RPE of 2-month-old *Abca4*$^{-/-}$ *Rdh8*$^{-/-}$ mice illuminated with 20-fs pulsed light. (**A**) Representative images of the RPE in the intact ex vivo eye. Images were obtained in 2.6 seconds with 5.5 mW. Laser pulse durations are indicated in each image. Dashed lines outline the locations where the fluorescence intensity profile was measured. Scale bars: 50 μm. (**B**) TPEF intensity profile from locations along the dashed lines shown in **A**. Measured fluorescence is plotted on the left vertical axis and the ratio of the fluorescence excited with 20-fs light to that excited with 75-fs light is plotted on right vertical axis. (**C**) TPEF as a function of excitation power. Solid circles represent measured data points, solid lines represent the linear data fit. Slopes of the lines are 2.11 for 75 fs and 2.05 for 20 fs.

acquired with shorter pulses (Figure 2C). Imaging conditions were chosen to avoid saturation of the pixels, which was more difficult to achieve in *Rpe65*$^{-/-}$ mice for all pulse durations because of the bright fluorescence associated with enlarged retinosomes located near the RPE cell membranes (indicated by yellow arrows in Figure 2C) (36). TPEF as a function of excitation pulse duration showed a steady decrease with increasing pulse durations in *Rpe65*$^{-/-}$ mice (Figure 2D), whereas TPEF from *Dko* mice saturated around 20 fs. The difference in the dependence of TPEF on excitation pulse duration between the 2 types of mice can be attributed to differences between their excitation spectra and the fact that spectra of pulses with wider bandwidths (shorter pulse durations) were shifted toward blue (Figure 2A). Therefore, fluorophores in these mouse models might react in different ways to increasing the excitation bandwidth. Thus, the $1/\tau$ dependence of TPEF on pulse duration is altered when the excitation bandwidth exceeds the width of the 2-photon absorption band or when spectral bandwidths of progressively shorter pulses spread across irregularities in the excitation spectrum (37–39). To confirm this supposition, the ratio of TPEF excited with pulses of 25 fs, 20 fs, and 18 fs to the TPEF excited with 35-fs pulses was numerically modeled by using the measured pulse and excitation spectra shown in Figure 2, A and B and a previously described method (39). The modeling results confirmed the experimental result, i.e., a steeper TPEF increase in *Rpe65*$^{-/-}$ mice than in *Dko* mice in response to reducing the pulse duration (Figure 2D).

TPEF from retinosomes in the RPE of Rpe65$^{-/-}$ *mice excited with 20-fs pulsed light*. *Rpe65*$^{-/-}$ mice represent a model of Leber congenital amaurosis (LCA) (17), a congenital human blinding disease. The impact of short pulses on TPEF imaging of the RPE in these mice was analyzed in detail (Figure 3). Fluorescence from retinosomes containing retinyl esters dominates RPE fluorescence. Under imaging conditions in which retinosomes do not saturate the detector, interior portions of RPE cells appear black (Figure 3A). Linear fluorescence profile traces through a section of the RPE revealed that the dynamic range of images is close to 250 gray pixel values, whereas the maximum dynamic range of the images throughout this study is 255 gray pixel values (Figure 3B). This observation indicates that the fluorescence signal from the brightest retinosomes might have been higher than that represented by their gray pixel values. With maximum fluorescence originating from retinosomes, and almost no fluorescence emanating from outside, the ratio of TPEF excited with 20-fs laser pulses to that excited with 75-fs varied from 2 to 3.4 between different retinosomes. This difference could indicate some heterogeneity in the composition of retinosomes, and possibly a nearly saturated signal in some. Fluorescence emission spectra from the RPE of these mice were the same whether probed with 20-fs or 75-fs light (Figure 3C), confirming that in both cases the image was formed by fluorescence generated from the same fluorophores.

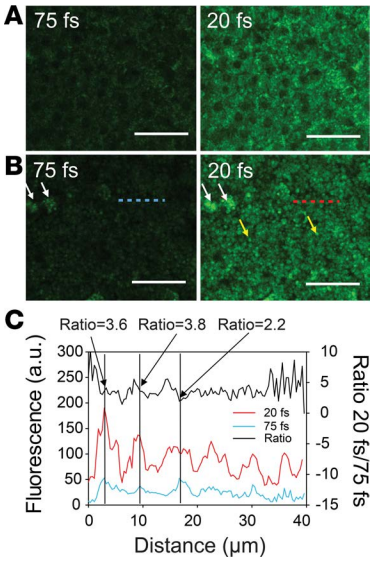

Figure 5. Impact of reducing pulse duration on TPEF from the retinas of 6-week-old *Abca4*$^{-/-}$ *Rdh8*$^{-/-}$ mice 3 days after initiation of photoreceptor-damaging stress. (**A**) Images of the RPE in the intact ex vivo eye. (**B**) Photoreceptor layer in the intact ex vivo eye. White arrows indicate macrophages; yellow arrows indicate enlarged photoreceptors (44). Dashed lines outline the locations where fluorescence intensity profile was measured. Images were obtained in 2.6 seconds with 4.4 mW. Scale bars (**A** and **B**): 50 μm. (**C**) TPEF intensity profile from locations along the dashed lines shown in **B**. Measured fluorescence is plotted on the left vertical axis and the ratios of fluorescence excited with 20-fs light to that excited with 75-fs light are plotted on right vertical axis.

Impact of short pulses on TPEF from the RPE and retina of Dko mice. *Dko* mice are an animal model of human Stargardt disease that exhibit many features of age-related macular degeneration (AMD) (40–43). Here, the potential of reducing laser power needed for imaging the RPE of these mice was evaluated. TPEF images of the RPE of *Dko* mice obtained with a 20-fs laser were brighter than those obtained with a 75-fs laser at the same center wavelength and laser power (Figure 4A). The ratio of mean gray pixel values generated by 20-fs and 75-fs light was on average 4.2, with a standard deviation of ±0.3. The dynamic range of these images was 170. As expected, fluorescence from the RPE of these mice was more uniformly distributed than in *Rpe65*$^{-/-}$ mice. The increase in fluorescence in response to short-pulse excitation also was evaluated by analyzing the fluorescence intensity profile along the linear traces. This revealed a fluorescence increase from bright granules equal to 3.4, slightly smaller than from the surrounding areas (Figure 4B). Fluorophores in the RPE of these mice responded to longer wavelengths of light than did *Rpe65*$^{-/-}$ mice, so TPEF signals in response to excitation with different levels of laser power were measured and plotted on a log-log scale. The slope of the linear fit through the data points was 2.1 for both 75-fs and 20-fs pulse durations (Figure 4C), confirming TPE.

Enlarged photoreceptors and the presence of macrophages are early signs of a degenerating retina and were visualized in this study after inducing photoreceptor damage in *Dko* mice (44). Images of the retina in *Dko* mice obtained with 20-fs laser pulses were brighter than those obtained with 75-fs laser pulses; the corresponding ratio of mean gray pixel values was 3.2 for the RPE and 3.8 for photoreceptors (Figure 5, A and B). Fluorescence intensity profiles revealed outlines of individual photoreceptors with diameters varying from 3 to 5 μm, consistent with a previous report (44) (Figure 5C). The ratio of fluorescence obtained with 20-fs laser pulses to that with 75-fs pulses varied for different photoreceptors, ranging from 2.2 to 3.8, possibly indicating different fluorophore content related to different stages of degeneration.

TPEF imaging of the retina in vivo with short laser pulses. The ratio of mean pixel values of retinal fluorescence obtained with 25-fs laser pulses to that with 75-fs pulses measured in live *Dko* mouse eyes was equal to 2.8 at 2, 3, and 4 days after induction of photoreceptor damage (Figure 6, A–C). An increase in brightness of the RPE in *Rpe65*$^{-/-}$ mice (Figure 6D) was also evident in images obtained in vivo. This increase was smaller than that obtained ex vivo in these mice, as well as that found in *Dko* mice. This difference could arise from the fact that fluorescence from *Rpe65*$^{-/-}$ mice has a maximum around 490 nm, whereas fluorescence from *Dko* mice has a maximum around 590 nm. Also, during in vivo measurements, fluorescence from the RPE travels through the photoreceptor layer, and a portion of it could be absorbed by the chromophores located in rod and cone photoreceptor cells. Moreover, with 75-fs excitation, there are areas devoid of fluorescence, which causes the mean pixel value of images obtained with 75-fs light pulses to be affected less by the secondary fluorescence absorption by chromophores present in photoreceptors.

Even though mouse rod photoreceptor outer segments are more challenging to image than human because their diameter is 1.1 μm as compared with 2 μm in humans, individual rod photoreceptor outer segments were visualized in vivo in 2-month-old mice expressing human rhodopsin–green fluorescent

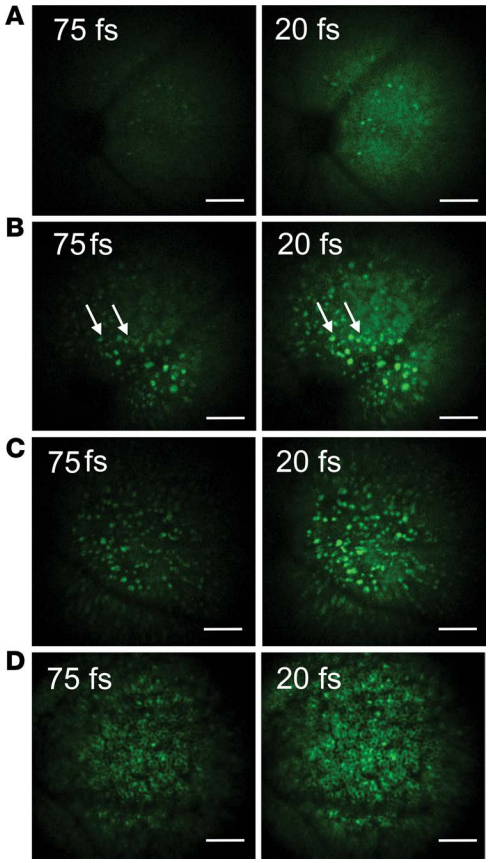

Figure 6. Impact of reduced pulse duration on in vivo TPEF imaging of the RPE and photoreceptor layers. In vivo images of the retina in 6-week-old *Abca4*$^{-/-}$ *Rdh8*$^{-/-}$ mice, on (**A**) day 2, (**B**) day 3, and (**C**) day 4 after inducing photoreceptor-damaging stress. Ratio of fluorescence excited with 20-fs light to that excited with 75-fs light was 2.8 on days 2, 3, and 4. White arrows indicate macrophages. (**D**) In vivo images of the retina in 1-year-old *Rpe65*$^{-/-}$ mice. Ratio of fluorescence excited with 20-fs light to that excited with 75-fs light was 1.7. Pulse durations are indicated in each image. Images were obtained with 6–10 mW in 2.6 seconds. Average laser power was kept at the same level for both images in **A**–**D**. Scale bars: 200 μm.

fusion protein (GFP) in photoreceptor outer segments after alignment of just 10 imaging frames (Supplemental Figure 3).

Towards TPEF imaging in humans: adaptive-optics 2-photon retinal imaging. Reducing laser pulse duration improves the efficiency of TPEF and offers the potential for application in humans. To obtain in vivo images of mouse RPE with minimal laser power of 1 mW (Figure 7), we employed (a) 20-fs laser pulses with dispersion compensation, (b) sensorless adaptive optics to optimize light focusing in the sample, and (c) image registration and averaging. Though fluorescent light was detected even in single frames, no biological structures were visible. Thus, up to 100 frames were collected with 75-fs, 32-fs, and 20-fs lasers. Clear images of individual RPE cells emerged after the averaging and registration of 100 single frames obtained with both 20-fs and 32-fs lasers (27). But only obscure traces of the RPE were visualized with the 75-fs laser. Moreover, clear images of individual RPE cells were already visible after registration and averaging of 40 frames obtained with the 2 ultrashort-pulsing lasers. Furthermore, no damage to the retina or RPE was detected after repetitive TPEF imaging.

Considering that TPEF can provide 3D volume images of the retina, allowing the study of the ganglion cells and the interactions between retinal neurons and the RPE, we obtained *Z*-stack images of the retina, revealing interplay between photoreceptor outer segments and the RPE (Figure 8 and Supplemental Videos 1, 2, and 3). Even though 3D volumes of the entire retina cannot be obtained within safety limits, the 3D volumes of portions of the retina such as the interface between photoreceptors and RPE are within reach.

Fluorescence lifetime imaging with short laser pulses. An additional advantage of using wide-bandwidth pulses is the ability to simultaneously excite fluorophores with different absorption spectra and to determine their subcellular distribution based on the differences in fluorescence lifetimes. Fluorescence lifetime imaging (FLIM) of the RPE in *Rpe65*$^{-/-}$ mice, which owing to the blockade of the retinoid cycle overaccumulate retinyl esters in the RPE and do not accumulate other retinoid-derived products (23), revealed one type of fluorescent granules with average fluorescence lifetime with a well-defined maximum around 2.5 ns (Figure 9A). In contrast, FLIM of RPE in *Abca4*$^{PV/PV}$ mice, which have a mutation in the ABCA4 transporter, displayed fluorescent granules with distinctly different average fluorescence lifetimes, ranging from 0.4 to 3.7 ns (Figure 9A). *Abca4*$^{PV/PV}$ mice comprise a new animal model that recapitulates many of

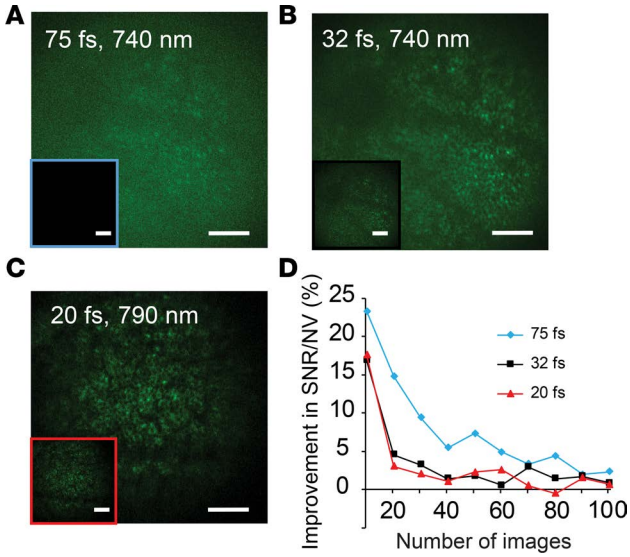

Figure 7. Improvement of in vivo TPEF images with decreased pulse durations. (**A**–**C**) Large images show the average of 100 images after registration. Each inset shows the average of 40 images. Images were collected with a pulse duration of 75 fs, 32 fs, and 20 fs, using an average laser power of (**A**) 1 mW, (**B**) 0.9 mW, and (**C**) 1 mW. Scale bars: 200 μm. (**D**) Graph shows the improvement in image quality as progressively more images are included in the averaged image. For the shorter pulse durations (30 fs and 20 fs), the amount of improvement in image quality quickly decreases as more images are included in the averaged image, indicating that fewer images need to be collected to achieve high-quality averaged images. SNR, signal-to-noise ratio; NV, normalized variance.

the important features of Stargardt disease in humans. The complex L541P;A1038V (PV) allele (2 missense changes, P and V, on the same allele) of *ABCA4* dramatically accelerates the initiation of the human retinopathy compared with other mutants in the *ABCA4* gene (45–47). Average fluorescence lifetimes from granules, distributed around the cell borders in $Abca4^{PV/PV}$ mice, shown in red in Figure 9A, ranged from 2.7 to 3.7 ns, probed with either 20-fs or 75-fs pulses. However, these granules appeared larger in images obtained with 20-fs as compared with those obtained with 75-fs pulses, or sometimes were not visible when imaging with 75-fs pulses. Furthermore, there were more pixels with the average fluorescence lifetime of 2 to 3.7 ns in images obtained with 20-fs as compared with 75-fs pulses (Figure 9B).

TPEF imaging with 20-fs pulses did not induce deterioration of the structure and function of the retina. To evaluate the impact of TPEF imaging on the structure and function of the retina we performed a variety of tests in mice that were either not exposed to light (NL), were exposed to bright white light (WL) as described in supplemental methods, or were exposed to TPEF imaging light with 20-fs pulses at 790 nm, 1.2 mW for the duration of 100 frames (IR). These IR conditions were more severe than those that suffice to obtain informative TPEF images, namely 40 frames and 1 mW (Figure 7, insets and panel D).

No impact of TPEF imaging on retinal structure was detected by SLO, OCT, and histology measurements. SLO imaging of the mouse fundus in vivo revealed that there were no statistical differences in the quantity of autofluorescent (AF) spots between mice exposed and not exposed to TPEF imaging in either of the tested mice: BALB/cJ (Figure 10A), albino *Dko* (Figure 10B), and pigmented *Dko* (Figure 10C). In contrast, there were significantly more AF spots in mice exposed to bright WL, in all 3 genotypes, even in BALB/cJ mice, which are much less sensitive to light-induced retinal damage. An increase in AF spots following exposure to light is indicative of macrophage infiltration and is associated with retinal degeneration (44, 48). Retinal morphology was assessed by OCT imaging in vivo (Figure 10) and by histology of enucleated eyes (Supplemental Figure 4). In BALB/cJ, albino *Dko*, and pigmented *Dko* there were no statistical differences in the thickness of outer nuclear layer (ONL), or nuclei count between mice exposed to NL and IR conditions. However, ONL thicknesses and nuclei counts were significantly reduced in albino *Dko* and pigmented *Dko* mice that were exposed to WL, but not in BALB/cJ mice, which are less prone to light-induced retinal damage than *Dko* mice.

In healthy retina, contents of visual pigment rhodopsin and 11-*cis*-retinal are maximal after dark adaptation (49), and reflect functioning retinoid visual cycle, photoreceptor cells, and the RPE (17). Thus, to assess the impact of TPEF imaging at the molecular level, we measured rhodopsin and 11-*cis*-retinal levels in dark-adapted mouse eyes. We did not observe any differences in the amounts of rhodopsin and 11-*cis*-retinal between mice exposed (IR) and not exposed to TPEF imaging (NL) in either of the tested mice: BALB/cJ (Supplemental Figure 5A), albino *Dko* (Supplemental Figure 5B), and pigmented *Dko* (Supplemental Figure 5C). However, there was significant damage to the retinoid visual cycle components in mice exposed to bright WL, even in BALB/cJ mice. Furthermore, there was no statistical difference in retinal function between mice exposed to either NL or IR conditions as assessed by electroretinogram (ERG)

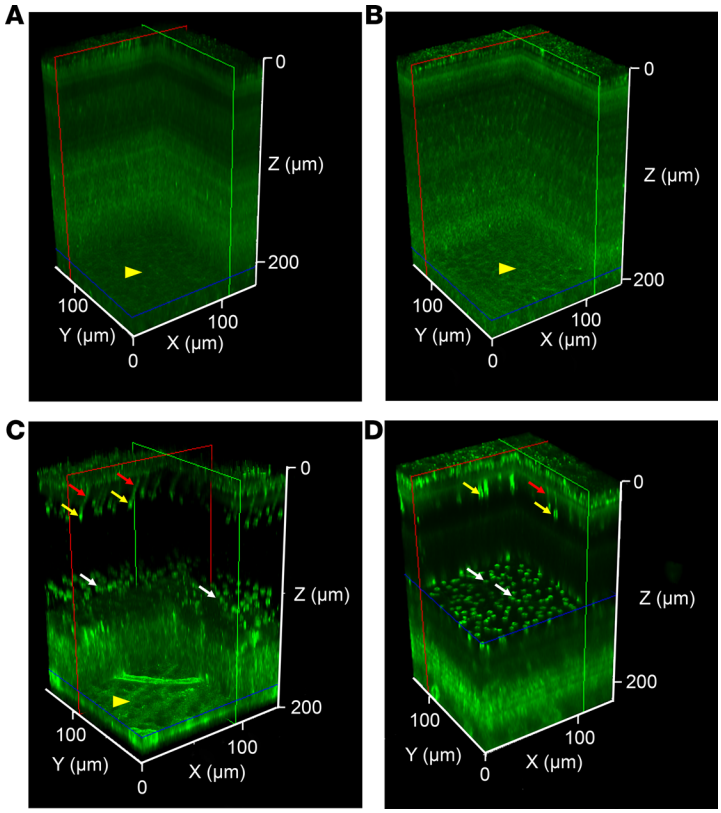

Figure 8. Arrangement of retinal cells in the intact mouse eye as visualized by 2-photon excitation fluorescence (TPEF) imaging with 20-fs laser pulses. Shown are 3D reconstructions of TPEF images, derived from *Z*-stacks of the retina and RPE in 2.5-month-old mice: (**A**) BALB/cJ mouse, (**B**) *Abca4*$^{-/-}$ *Rdh8*$^{-/-}$ mouse, (**C**) BALB/cJ mouse, 50 hours after intravitreal injection of rhodamine-tagged peanut agglutinin (PNA) and (**D**) BALB/cJ mouse, 50 hours after intravitreal injection of fluorescein-tagged PNA (see supplemental methods). Images were obtained with 20-fs laser pulses and a 1.0 numerical aperture (NA) objective. Green frames indicate sections in the *X*-*Z* plane, red frames indicate sections in the *Y*-*Z* plane and blue frames indicate sections in the *X*-*Y* plane. In each section the RPE is at the top of the 3D image, at *Z* = 0 μm. Cone outer segment sheaths are indicated with red arrows, cone inner segments with yellow arrows, cone pedicles with white arrows, and the ganglion cell layer with yellow arrowheads.

measurements (50). Whereas both a-wave and b-wave scotopic ERG amplitudes were significantly reduced in both albino *Dko* and pigmented *Dko* mice, no significant difference was observed in BALB/cJ mice that were exposed to WL (Figure 11).

To assess the degree of stress to the retina at the cellular level following exposure to light, we performed immunohistochemistry to observe any changes in glial fibrillary acidic protein (GFAP) as a measure of Müller cell gliosis (51), and the tight junction protein zonula occludens-1 (ZO-1) to evaluate the integrity and shape of RPE cells (52). Gliosis was not detected in mice exposed to either NL or IR conditions (Supplemental Figure 6). However, after exposure to WL we observed mild gliosis in BALB/cJ mice (Supplemental Figure 6A) and severe gliosis in albino and pigmented *Dko* mice (Supplemental Figure 6, B and C). Furthermore, the arrangement and integrity of RPE cells were not altered in either of the mouse models after exposure to TPEF imaging conditions (Supplemental Figure 7).

Discussion

Ophthalmology and the visual sciences have been revolutionized by the development of imaging techniques such as SLO (3, 53, 54) and OCT (2, 55–57), which improved the detection of certain pathological conditions associated with retinal diseases (1, 58). In parallel with innovations in imaging, experimental therapies also have advanced (59–61). As gene transfer techniques and genetic manipulations evolve along with the implantation of progenitor cells, high-resolution imaging techniques together with physiological measurements will become essential for evaluating the efficacy of these treatment options. Among the next generation of imaging modalities, TPEF is one of the most promising because it can, with or without artificial fluorescent markers, track light-induced changes in the eye by recording signals from native retinoids, endogenous fluorescent molecules that are essential components of visual processing. Sustaining the eye's ability to sense light requires the continuous replenishment of retinoids, and their normal processing reflects the health of the retina. However, retinoids also can form toxic condensation products that accumulate in the retina with age and in many retinal diseases (62, 63). Because retinoids are chemically unstable upon UV/Vis illumination, and because the front of the human eye does not transmit light up to 400 nm, TPEF-based imaging offers the opportunity to visualize different stages of retinoid processing and thus detect certain forms of retinal degeneration at their earliest stages as well as to determine the efficacy of therapies aimed at preventing or resolving these defects.

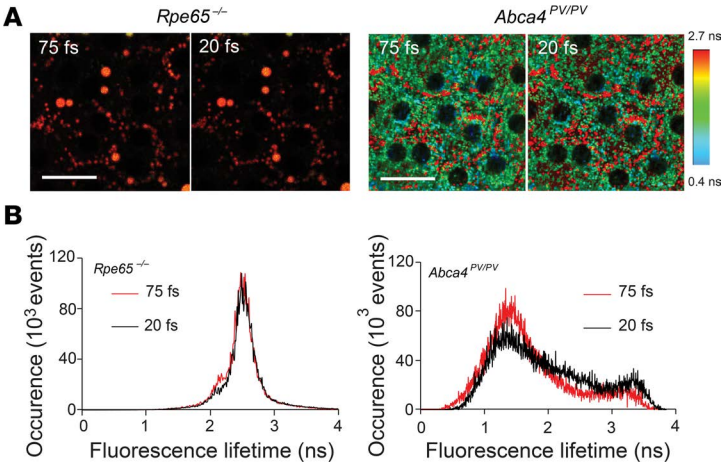

Figure 9. Fluorescence lifetime imaging (FLIM) with 2-photon excitation with wide-bandwidth pulses reflects differences in subcellular distribution of endogenous fluorophores in the RPE of dual-knockin (*Abca4*$^{PV/PV}$) mice. (**A**) Images of the RPE in *Rpe65*$^{-/-}$ and *Abca4*$^{PV/PV}$ mice were obtained without staining or artificial dye. The colors are based on the average fluorescence lifetime for each pixel. Scale bars: 25 μm. Color scale shown on the right is the same for all images. (**B**) Histograms of average fluorescence lifetimes for each pixel of images shown in **A** revealed overlapping maxima between 2.48 ns and 2.55 ns for data collected with 20-fs and 75-fs pulses in *Rpe65*$^{-/-}$ mice. In *Abca4*$^{PV/PV}$ mice, larger quantities of pixels with average fluorescence lifetime in the range of 2 to 3 ns were present in data obtained with 20 fs.

Several problems need to be overcome before this new methodology can be safely adapted for human use. Increasing the signal while using lower laser energy to avoid potential toxicity during imaging is a major needed advance. Aside from using highly sensitive detectors and improved laser beam focusing achieved with customized objectives and adaptive optics (25), we demonstrated that the TPEF signal can be maximized by optimizing laser pulse duration.

Here we present, for the first time to our knowledge, low laser exposure, noninvasive TPEF imaging of the retina in vivo, resulting from the application of ultrashort laser pulses coupled with high-order dispersion compensation. A reduced laser pulse duration is associated with an increased spectral bandwidth; thus, dispersion introduced by optical components of the imaging system (64) results in stretching laser pulses in the time domain at the imaged sample. This physical process results in stretching laser pulses in the time domain at the imaged sample. Here, to achieve temporal focusing at the retina, phases of the spectral components of laser light were individually altered by the SLM after spatial splitting and diffraction by a diffraction grating. After characterizing the dispersion associated with the system, a customized MIIPS (35) was incorporated to restore a short pulse duration at the sample plane. This was confirmed by measuring 20-fs pulses on the outputs of the laser and the microscope objective. In live mouse eyes an approximately 3-fold increase in TPEF was obtained with 20-fs laser pulses as compared with that obtained with 75-fs pulses (Figure 6). In view of translating this technology towards imaging the human eye, where eye dimensions can vary considerably between individuals, we estimated that 16-fs Fourier transform–limited pulses became 22 fs if the same MIIPS mask was used for eyes differing by ±5 mm from the 24-mm axial length (65), considering that dispersion of the vitreous humor is close to that of water (66, 67). As expected, longer pulses spread less than shorter pulses. For very short pulses, MIIPS masks can be generated based on different path lengths in water and dimension of the subject eye.

Two-photon FLIM has been used to visualize exogenous fluorophores in living mice (68). An additional advantage of using wide-bandwidth pulses is the ability to visualize the subcellular distribution of endogenous fluorophores, markers of the health of retinal biochemical processes, based on FLIM (Figure 8) (69). Retinyl esters are not excited efficiently with 790-nm or longer wavelengths, whereas retinal condensation products are optimally excited with 780- to 850-nm light (Figure 2B). Moreover, when imaging RPE in vivo, eye tissue motion artifacts make determination of the relative localization of different fluorophores difficult. Thus, FLIM with wide-bandwidth laser pulses, such as that shown in Figure 2A, could detect the distribution of both types of retinoids in vivo.

Recent advances in TPEF imaging resulted in elucidation of a succession of steps leading to retinal degeneration following bright light exposure (44). However, only very low laser power can be used to translate these advances safely to obtain TPEF images of human retina. Unfortunately, reduction in laser power also reduces the signal-to-noise ratio of collected images, making it difficult to visualize structural details. Here, image registration and averaging methods applied to TPEF images of the endogenous fluorophores in living animals were combined with sensorless adaptive optics and reduced laser pulse durations to show that information about the subcellular distribution of vitamin A metabolites can be obtained with laser power below 1 mW. As the pulse duration was reduced from 75 fs to 32 fs and 20 fs, the structure of the

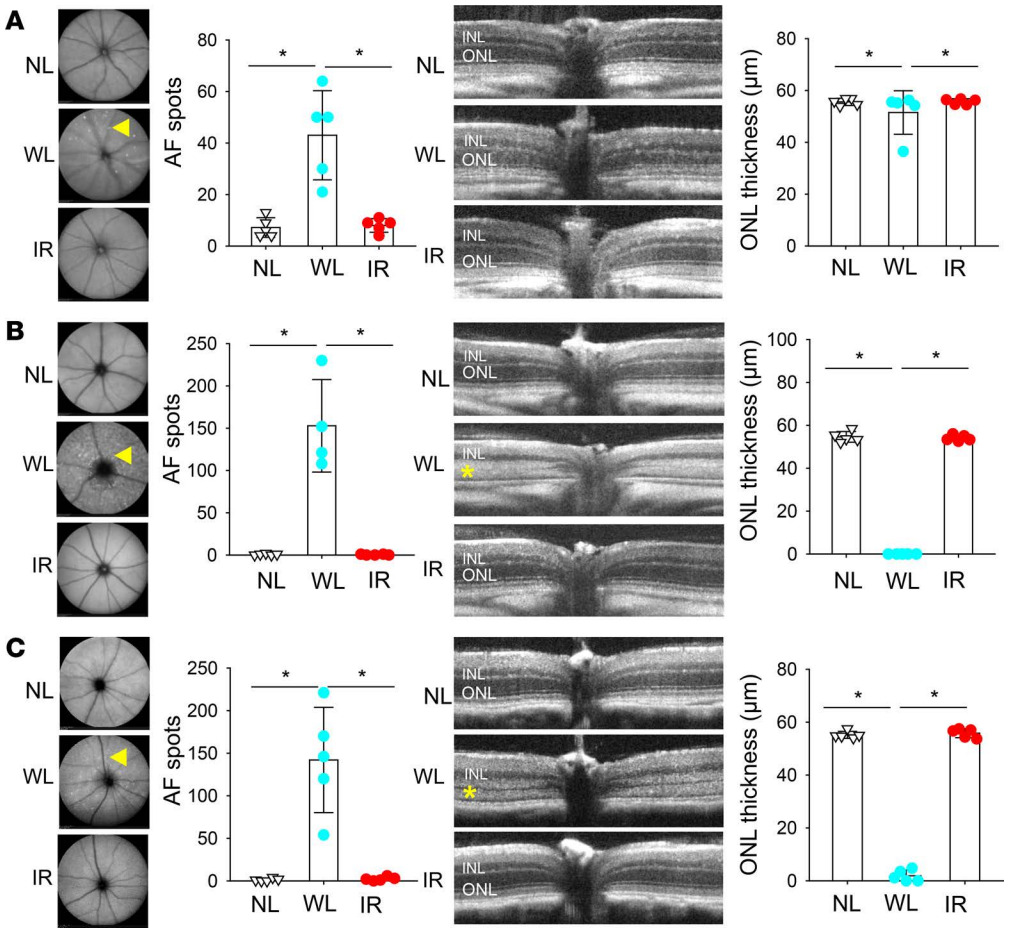

Figure 10. No impact of TPEF imaging light on retinal structure was detected by SLO and OCT. BALB/cJ mice, $n = 5$ for each group (**A**), albino *Abca4*$^{-/-}$ *Rdh8*$^{-/-}$ (*Dko*) mice, $n = 4–5$ for each group (**B**), and pigmented *Dko* mice, $n = 5$ for each group (**C**) were either exposed to photoreceptor-damaging white light (WL), not exposed to light (NL), or exposed to TPEF imaging light (IR). Representative SLO images are shown in the left column, yellow arrowheads are designating autofluorescent (AF) spots indicative of macrophages. Quantification of AF spots in SLO images is shown in the second column. Representative OCT images from each group are shown in the third column, where yellow stars indicate lack of visible outer nuclear layer (ONL), indicative of photoreceptor damage. INL indicates inner nuclear layer. Analysis of the thickness of ONL for each group is shown in rightmost column. All mice were 1–2 months old. Data are shown as means ± SD. *$P < 0.001$ by 1-way ANOVA with Bonferroni's post hoc test.

RPE mosaic became increasingly visible. Moreover, fewer images had to be collected to obtain information-rich data, further reducing the exposure to laser light.

Considering the TPE spectra of retinal fluorophores (Figure 2), doubling the improvement in TPEF cannot be achieved by further reducing the pulse duration to 10 fs, because this would increase the pulse spectral bandwidth to approximately 100 nm (37), thereby placing a substantial portion of the excitation pulse spectral components outside the excitation bandwidth of certain retinoid derivatives (Figure 2). Improved efficiency of TPE by reducing the PRF and concomitantly increasing the pulse peak energy density can be achieved by either cavity damping or pulse picking (70), or with the use of regenerative amplifiers (71). However, with considerably reduced PRF, as provided by regenerative amplifiers, the number of pulses per pixel could become 1 or lower; thus, the signal variation from pixel to pixel could be related to differences in the quantity of pulses ± 100%, overshadowing the image contrast provided by differences in fluorophore distribution. Theer et al. addressed this problem by synchronizing the regenerative amplifiers with the clock of the imaging system. But even with these modifications, the maximum *X-Y* size of imaged tissue was only 200 μm by 200 μm. Moreover, with the considerable reduction in PRF, the energy density per pulse increased by more than 10^3 times, raising concern about the safety of imaging the retina in vivo (72). Lower energy density and fast image acquisition rates over a limited 100 × 100 μm area of an artificial sample were achieved by combining wavefront, sensorless adaptive optics with wide-field 2-photon microscopy (73). However, both a larger imaging area and the ability to excite native fluorophores are critical to quantify and track lesions in retinal processes (27). Karpf et al. employed 500-ps pulses with 1,064-nm center wavelength at 400-kHz PRF and a commercial microscope equipped with 0.8-NA objective (74). They obtained images of *Convalaria majalis* stained with acridine orange at sufficient 5 μs/pixel imaging speed. However, they needed to use 135 mW of average power to achieve good quality images. A longer wavelength such as 1,064 nm could allow imaging of retinal structures by 3-photon excitation (75). To apply their approach towards noninvasive imaging of the retina would require their pulse duration to be reduced approximately 1,000 times. In addition, this approach must be carefully evaluated for safety because with substantial reduction of the PRF, each pulse would carry proportionally more energy.

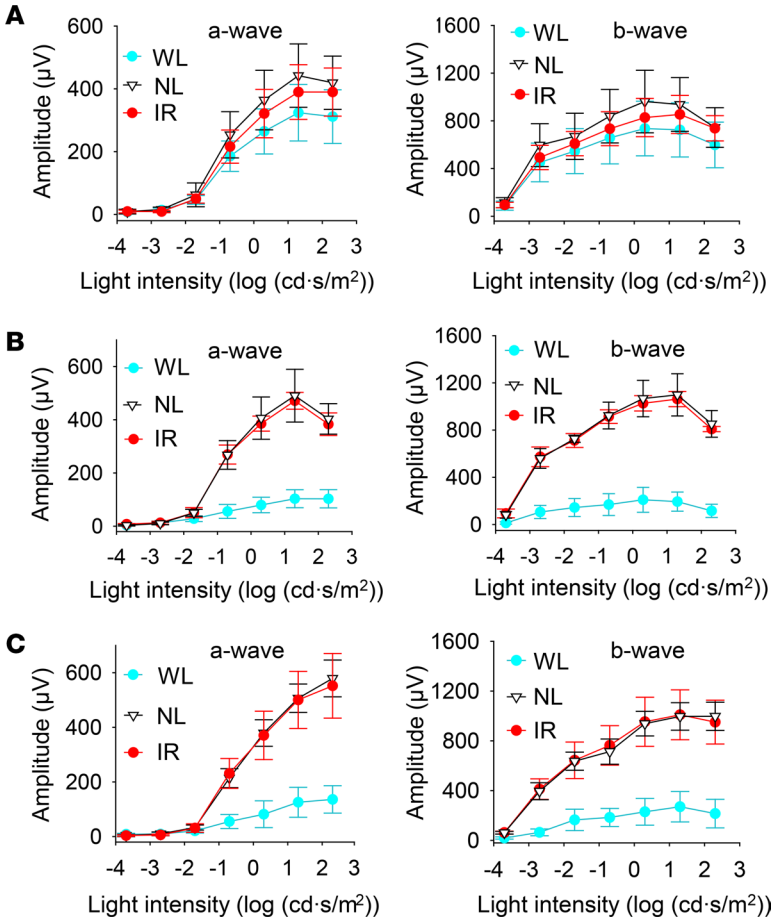

Figure 11. Retinal function was not affected by exposure to TPEF imaging light. BALB/cJ mice, n = 7 for each group (**A**), albino *Abca4*$^{-/-}$ *Rdh8*$^{-/-}$ (*Dko*) mice, n = 5–6 for each group (**B**), and pigmented *Dko* mice, n = 5 for each group (**C**) were either exposed to photoreceptor-damaging white light (WL), not exposed to light (NL), or exposed to TPEF imaging light (IR). Scotopic ERG amplitudes were measured as a function of variable light intensity flashes. Data are shown as means ± SD. In albino *Dko* (**B**) and pigmented *Dko* (**C**) for each flash brighter than –1 for a-wave and –3 (log[cd·s/m²]) for b-wave, there were significant differences in scotopic amplitudes between mice subjected to WL and IR, and mice subjected to WL and NL, with $P < 0.001$ by ANOVA with Bonferroni's post hoc test. There were no statistical differences between WL, NL, and IR groups in BALB/cJ mice (**A**). All mice were 1–2 months old.

Previously, 2-photon images of the retina were not achieved within the safety limits prescribed by the American National Standard for Safe Use of Lasers, ANSI Z136.1 – 2014. Moreover, potentially deleterious changes occurred to the retina following exposure to pulsed IR light at just 75% of light levels permissible by current safety standards (76). In our present study, informative images of mouse RPE in vivo were obtained in 50 seconds with 1 mW of average power. Considering the differences in NAs between human and mouse eyes (0.22 vs. 0.49) (77), in vivo images presented here were obtained with less than 30% of the maximum permissible exposure limit (see supplemental methods). The use of 20-fs pulses also needed to be evaluated for the safety of single pulses. We calculated the maximum permissible average light power per single pulse limit and obtained a value of 680 mW (72), well above the average power used in this study. Furthermore, our pulse peak power, approximately 588 W, assuming a Gaussian pulse and 1 mW of average power, was well below the critical power thresholds for self-focusing (78, 79) and plasma formation calculated for 20-fs pulses: 1.5 MW and 159 kW, respectively (76). Therefore, the work reported here provides a foundation for obtaining informative 2-photon microscopy images with laser exposures below damage thresholds per current safety standards. Furthermore, using a variety of tests, including in vivo imaging, ERG measurements, histology, immunohistochemistry, and the quantification of visual pigment and visual chromophore, no deleterious changes to the structure and function of the retina occurred after exposure to 20-fs, 790-nm TPE imaging light. However, the impact of reducing PRF and pulse duration on retinal safety needs further evaluation before this technology can be applied to humans.

In conclusion, we demonstrate noninvasive TPEF imaging of the retina in vivo for the first time to our knowledge, resulting from the application of ultrashort laser pulses coupled with high-order dispersion compensation. By introducing a laser delivering 20-fs pulses with precise dispersion compensation, a greater than 3-fold increase in TPEF of endogenous retinal fluorophores was achieved as compared with a 75-fs pulsing laser at the same average power and center wavelength. Moreover, clear subcellular images of the RPE in live mouse models were achieved with 790-nm and 1-mW laser light in less than 60 seconds with a field of view larger than 1 mm × 1 mm. Application of 20-fs pulses allows informative images to

be obtained of tissue layers deep within the posterior segment of the eye, namely the RPE, with minimal laser power. Furthermore, wide bandwidth of short pulses enables excitation of multiple fluorophores with different absorption spectra and thus can provide information about their relative changes in intracellular content and distribution, reflecting the metabolic status of the retina. This work represents important progress towards safe, noninvasive imaging of biochemical processes in the human retina applicable to the study of retinal health, disease, and therapeutic intervention.

Methods

Mice. All mice were housed in the Animal Resource Center at the School of Medicine, Case Western Reserve University, where they were maintained on a normal mouse chow diet under complete darkness for at least 24 hours before procedures or in a 12-hour light (~10 lux)/12-hour dark cyclic environment. Before indicated procedures, mice were anesthetized with an intraperitoneal (i.p.) injection with a solution of ketamine (20 mg/ml) and xylazine (1.75 mg/ml) diluted with 10 mM sodium phosphate, pH 7.2, containing 100 mM NaCl, at a dose of 0.10–0.13 ml/25 g body weight. Before imaging, mouse pupils were dilated with 1.0% tropicamide ophthalmic solution (Akron, Inc.). Male and female 1- to 3-month-old BALB/cJ mice were obtained from The Jackson Laboratory. *Abca4*$^{-/-}$ *Rdh8*$^{-/-}$ (*Dko*) mice were generated and genotyped as previously described (80) and mixed sexes of 1- to 2-month-old mice were used for the present study. Albino *Dko* and *Rpe65*$^{-/-}$ mice were generated as previously described and mixed sexes of 1- to 12-month-old mice were used for the present study (23, 81, 82). Human opsin–green fluorescent protein (GFP) fusion knockin *hrhoG*/*hrhoG* mice were albinos and were generated as previously described (23, 81, 82); 2-month-old mice were used in this study. Dual-knockin, *Abca4*$^{PV/PV}$ mice, were generated as previously described (45); 2-month-old mice were used in this study.

A 2-photon system for imaging the retina in vivo with reduced laser power. To increase the TPEF signal and to minimize laser light exposure needed to obtain informative images of the retina, an adaptive-optics 2-photon imaging system was redesigned and equipped with new light sources delivering short laser pulses and a dispersion compensation system capable of compensating for higher order dispersion. After passing through a dispersion compensation system, laser light was attenuated in a controlled, variable manner by using an EOM. Ocular aberrations were corrected with a custom, sensorless adaptive-optics system (25), employing a software algorithm based on image quality metric feedback as outlined in supplemental methods. The horizontal scanning beam operated at a 400- to 700-Hz line frequency that, together with vertical beam scanning, spanned 512 by 512 pixels at 1.3 seconds per frame. To minimize sample exposure to laser light while detection was in the idle state, the EOM switched off the excitation beam for half of the period of the horizontal scan and at the turn of each vertical and horizontal scan, yielding a 30% duty cycle. To deliver TPE light to the retina and to collect the emanating fluorescence, a 0.25-NA 10× objective (Leica Microsystems Inc.) with an NA close to the human NA (83), equal to approximately 0.2 for a pupil diameter of 6 mm, was used for imaging the eye ex vivo, whereas a custom periscope objective designed for noninvasive imaging of the retina was employed in live mice (77). For ex vivo imaging, enucleated, intact mouse eyes were submerged in phosphate–buffered saline (PBS) composed of 9.5 mM sodium phosphate, 137 mM NaCl and 2.7 mM KCl, pH 7.4, and the eye surface was submerged approximately 3–4 mm below the surface of the solution. For in vivo imaging, an anesthetized mouse was surrounded by a heating pad and placed on a mechanical stage with its eye covered with GenTeal gel and a thin 3.2 mm diameter, 0 diopter contact lens (Cantor and Nissel) to avoid drying the cornea. To evaluate the impact of pulse duration on the efficiency of TPE a pulsed laser beam was introduced from (a) a wavelength-tunable, Vision S laser (Coherent) that delivered 75-fs pulses; (b) an Integral Element laser (Spectra Physics), which produced 32-fs pulses at 740 nm; and (c) a wavelength- and pulse duration–tunable Vitara T laser (Coherent) that provided pulses as short as 20 fs. All 3 lasers operated at an 80 MHz PRF. To ensure accurate comparison of TPE efficiencies in living animals between differing pulse durations, a switching mechanism was implemented that required less than 30 seconds to change from a laser delivering 75-fs excitation to those delivering either 20-fs or 32-fs excitation pulses. However, a considerably longer switching time was needed to change between the Integral Element (32 fs) and Vitara T lasers, because of substantial differences in the spectra of these 2 lasers and the resulting differences in the components of the dispersion compensation system. Dispersion compensation based on a prism pair, commercially available at Coherent and integrated with Vision S, restored a 75-fs pulse duration at the sample. However, 32-fs and 20-fs pulses required a more advanced method. A dispersion compensation of 740-nm, 32-fs light was initially attempted with a system

based on chirped mirrors (Supplemental Figure 1) but failed to produce satisfactory results. To precompensate for all dispersion terms, a custom diffraction grating and SLM-based MIIPS system (Biophotonics Solutions Inc.) (35) was incorporated. A critical design parameter for this custom MIIPS was 27,000 fs^2 of GDD in the 2-photon microscope including adaptive optics, EOM, and custom objectives.

Pulse durations were calculated based on measurements of the ACF using a Carpe autocorrelator (APE). The autocorrelator consisted of a Michelson interferometer with a variable length of one of its arms and 2 photodetectors, internal and external. A pulse duration measurement was possible at 2 locations, first where the main autocorrelator body (internal detector) was placed, and second, at the position of the external detector where the imaged sample was located.

Laser power measurements were performed with a power meter PM100D (Thorlabs), with EOM operating at either a 30% duty cycle for imaging or a 100% duty cycle for fluorescence measurements as a function of laser power and comparison of TPE at different pulse durations.

Excitation light spectra were measured with a USB4000 spectrometer (Ocean Optics).

FLIM. To obtain FLIM data, the photon counting signal from the nondescanned detector (Figure 1) was used. A trigger diode, placed just after the beamsplitter located in front of the EOM, provided synchronization signal between the laser pulses and the PicoHarp 300, the time-correlated single-photon counting module (PicoQuant). Photon counting was set to achieve maximum of 1,000 counts per pixel.

Statistics. Data from at least 3 independent experiments are presented as means ± standard deviations (SD). Analysis of variance (ANOVA) with Bonferroni's post hoc testing was used to determine differences between treatments. $P \leq 0.05$ was considered significant.

Study approval. Studies in animals were reviewed and approved by the Case Western Reserve University, School of Medicine Institutional Animal Care and Use Committee, located in Cleveland, Ohio. All animal procedures conformed to both the recommendations of the American Veterinary Medical Association Panel on Euthanasia and the Association for Research in Vision and Ophthalmology (Assurance number A-3145-01).

Data availability. The authors declare that all data supporting the findings of this study are available within the paper and supplemental information.

Author contributions

GP and KP designed the study. GP, PS, NA, MW, and KP designed experiments and analyzed the data. GP, PS, NA, ZD, DS, AES, DR, SS, and EHC performed experiments. All authors contributed to writing and editing the manuscript.

Acknowledgments

We acknowledge the contribution from T. Michael Redmond (NIH) for *Rpe65*$^{-/-}$ mice and John H. Wilson (Baylor College of Medicine) for human opsin–GFP fusion, knockin *hrhoG/hrhoG* mice. This research was supported in part by grants from the NIH (EY027283, U01 EY025451, R24 EY024864, EY11373 [Core Grant], and S10-OD016164 [CWRU SOM Light Microscopy Core Facility]). M. Wojtkowski and P. Stremplewski would like to acknowledge the European Union's Horizon 2020 research and innovation programme grant no. 666295 and the project no. TEAM TECH/2016-3/20 carried out within the TEAM-TECH programme of the Foundation for Polish Science cofinanced by the European Union under the European Regional Development Fund.

Address correspondence to: Krzysztof Palczewski, Department of Pharmacology, School of Medicine, Case Western Reserve University, 2109 Adelbert Road, Cleveland, Ohio 44106, USA. Phone: 216.368.4631, Email: kxp65@case.edu. Or to: Maciej Wojtkowski, Department of Physical Chemistry of Biological Systems, Institute of Physical Chemistry, Polish Academy of Sciences, Kasprzaka Str. 44/52, 01-224 Warsaw, Poland. Phone: 48.22.343.3283; Email: mwojtkowski@ichf.edu.pl.

1. Jacobson SG, et al. Gene therapy for leber congenital amaurosis caused by RPE65 mutations: safety and efficacy in 15 children and adults followed up to 3 years. *Arch Ophthalmol*. 2012;130(1):9–24.
2. Huang D, et al. Optical coherence tomography. *Science*. 1991;254(5035):1178–1181.
3. Webb RH, Hughes GW, Delori FC. Confocal scanning laser ophthalmoscope. *Appl Opt*. 1987;26(8):1492–1499.
4. Choma M, Sarunic M, Yang C, Izatt J. Sensitivity advantage of swept source and Fourier domain optical coherence tomography.

Opt Express. 2003;11(18):2183–2189.
5. Strauss RW, et al. The natural history of the progression of atrophy secondary to Stargardt disease (ProgStar) studies: Design and baseline characteristics: ProgStar Report No. 1. *Ophthalmology*. 2016;123(4):817–828.
6. Schroeder M, Kjellström U. Full-field ERG as a predictor of the natural course of ABCA4-associated retinal degenerations. *Mol Vis*. 2018;24:1–16.
7. Pfau M, et al. Green-light autofluorescence versus combined blue-light autofluorescence and near-infrared reflectance imaging in geographic atrophy secondary to age-related macular degeneration. *Invest Ophthalmol Vis Sci*. 2017;58(6):BIO121–BIO130.
8. Hillmann D, Spahr H, Pfäffle C, Sudkamp H, Franke G, Hüttmann G. In vivo optical imaging of physiological responses to photostimulation in human photoreceptors. *Proc Natl Acad Sci USA*. 2016;113(46):13138–13143.
9. Zhang P, et al. In vivo optophysiology reveals that G-protein activation triggers osmotic swelling and increased light scattering of rod photoreceptors. *Proc Natl Acad Sci USA*. 2017;114(14):E2937–E2946.
10. Kiser PD, Golczak M, Palczewski K. Chemistry of the retinoid (visual) cycle. *Chem Rev*. 2014;114(1):194–232.
11. Palczewski K. G protein-coupled receptor rhodopsin. *Annu Rev Biochem*. 2006;75:743–767.
12. Saari JC. Biochemistry of visual pigment regeneration: the Friedenwald lecture. *Invest Ophthalmol Vis Sci*. 2000;41(2):337–348.
13. Redmond TM, et al. Rpe65 is necessary for production of 11-cis-vitamin A in the retinal visual cycle. *Nat Genet*. 1998;20(4):344–351.
14. Arshavsky VY, Lamb TD, Pugh EN. G proteins and phototransduction. *Annu Rev Physiol*. 2002;64:153–187.
15. Tang PH, Kono M, Koutalos Y, Ablonczy Z, Crouch RK. New insights into retinoid metabolism and cycling within the retina. *Prog Retin Eye Res*. 2013;32:48–63.
16. von Lintig J, Kiser PD, Golczak M, Palczewski K. The biochemical and structural basis for trans-to-cis isomerization of retinoids in the chemistry of vision. *Trends Biochem Sci*. 2010;35(7):400–410.
17. Kiser PD, Palczewski K. Retinoids and retinal diseases. *Annu Rev Vis Sci*. 2016;2:197–234.
18. Delori FC, Goger DG, Dorey CK. Age-related accumulation and spatial distribution of lipofuscin in RPE of normal subjects. *Invest Ophthalmol Vis Sci*. 2001;42(8):1855–1866.
19. Hammer M, Roggan A, Schweitzer D, Müller G. Optical properties of ocular fundus tissues--an in vitro study using the double-integrating-sphere technique and inverse Monte Carlo simulation. *Phys Med Biol*. 1995;40(6):963–978.
20. Denk W, Strickler JH, Webb WW. Two-photon laser scanning fluorescence microscopy. *Science*. 1990;248(4951):73–76.
21. Zipfel WR, Williams RM, Christie R, Nikitin AY, Hyman BT, Webb WW. Live tissue intrinsic emission microscopy using multiphoton-excited native fluorescence and second harmonic generation. *Proc Natl Acad Sci USA*. 2003;100(12):7075–7080.
22. Boettner EA, Wolter JR. Transmission of the ocular media. *Invest Ophthalmol Vis Sci*. 1962;1:776–783.
23. Palczewska G, et al. Noninvasive multiphoton fluorescence microscopy resolves retinol and retinal condensation products in mouse eyes. *Nat Med*. 2010;16(12):1444–1449.
24. Entenberg D, et al. Setup and use of a two-laser multiphoton microscope for multichannel intravital fluorescence imaging. *Nat Protoc*. 2011;6(10):1500–1520.
25. Palczewska G, et al. Noninvasive two-photon microscopy imaging of mouse retina and retinal pigment epithelium through the pupil of the eye. *Nat Med*. 2014;20(7):785–789.
26. Sharma R, Schwarz C, Hunter JJ, Palczewska G, Palczewski K, Williams DR. Formation and clearance of all-trans-retinol in rods investigated in the living primate eye with two-photon ophthalmoscopy. *Invest Ophthalmol Vis Sci*. 2017;58(1):604–613.
27. Alexander NS, Palczewska G, Stremplewski P, Wojtkowski M, Kern TS, Palczewski K. Image registration and averaging of low laser power two-photon fluorescence images of mouse retina. *Biomed Opt Express*. 2016;7(7):2671–2691.
28. Biss DP, et al. In vivo fluorescent imaging of the mouse retina using adaptive optics. *Opt Lett*. 2007;32(6):659–661.
29. Hunter JJ, et al. Images of photoreceptors in living primate eyes using adaptive optics two-photon ophthalmoscopy. *Biomed Opt Express*. 2010;2(1):139–148.
30. Geng Y, et al. Adaptive optics retinal imaging in the living mouse eye. *Biomed Opt Express*. 2012;3(4):715–734.
31. Cua M, et al. Coherence-gated sensorless adaptive optics multiphoton retinal imaging. *Sci Rep*. 2016;6:32223.
32. Rossi EA, et al. In vivo imaging of retinal pigment epithelium cells in age related macular degeneration. *Biomed Opt Express*. 2013;4(11):2527–2539.
33. Vogel CR, Arathorn DW, Roorda A, Parker A. Retinal motion estimation in adaptive optics scanning laser ophthalmoscopy. *Opt Express*. 2006;14(2):487–497.
34. Pervak V, Naumov S, Krausz F, Apolonski A. Chirped mirrors with low dispersion ripple. *Opt Express*. 2007;15(21):13768–13772.
35. Lozovoy VV, Pastirk I, Dantus M. Multiphoton intrapulse interference. IV. Ultrashort laser pulse spectral phase characterization and compensation. *Opt Lett*. 2004;29(7):775–777.
36. Orban T, Palczewska G, Palczewski K. Retinyl ester storage particles (retinosomes) from the retinal pigmented epithelium resemble lipid droplets in other tissues. *J Biol Chem*. 2011;286(19):17248–17258.
37. Xi P, Andegeko Y, Pestov D, Lovozoy VV, Dantus M. Two-photon imaging using adaptive phase compensated ultrashort laser pulses. *J Biomed Opt*. 2009;14(1):014002.
38. Xu C, Webb WW. Measurement of two-photon excitation cross sections of molecular fluorophores with data from 690 to 1050 nm. *J Opt Soc Am B*. 1996;13(3):481–491.
39. Pang S, Yeh AT, Wang C, Meissner KE. Beyond the 1/Tp limit: two-photon-excited fluorescence using pulses as short as sub-10-fs. *J Biomed Opt*. 2009;14(5):054041.
40. Maeda A, et al. Primary amines protect against retinal degeneration in mouse models of retinopathies. *Nat Chem Biol*. 2011;8(2):170–178.
41. Allikmets R, et al. Mutation of the Stargardt disease gene (ABCR) in age-related macular degeneration. *Science*. 1997;277(5333):1805–1807.
42. Rattner A, Smallwood PM, Nathans J. Identification and characterization of all-trans-retinol dehydrogenase from photoreceptor outer segments, the visual cycle enzyme that reduces all-trans-retinal to all-trans-retinol. *J Biol Chem*. 2000;275(15):11034–11043.

43. Parmar T, Parmar VM, Arai E, Sahu B, Perusek L, Maeda A. Acute stress responses are early molecular events of retinal degeneration in Abca4$^{-/-}$Rdh8$^{-/-}$ mice after light exposure. *Invest Ophthalmol Vis Sci*. 2016;57(7):3257–3267.
44. Maeda A, et al. Two-photon microscopy reveals early rod photoreceptor cell damage in light-exposed mutant mice. *Proc Natl Acad Sci USA*. 2014;111(14):E1428–E1437.
45. Zhang N, et al. Protein misfolding and the pathogenesis of ABCA4-associated retinal degenerations. *Hum Mol Genet*. 2015;24(11):3220–3237.
46. Rivera A, et al. A comprehensive survey of sequence variation in the ABCA4 (ABCR) gene in Stargardt disease and age-related macular degeneration. *Am J Hum Genet*. 2000;67(4):800–813.
47. Cideciyan AV, et al. ABCA4 disease progression and a proposed strategy for gene therapy. *Hum Mol Genet*. 2009;18(5):931–941.
48. Kohno H, et al. Photoreceptor proteins initiate microglial activation via Toll-like receptor 4 in retinal degeneration mediated by all-trans-retinal. *J Biol Chem*. 2013;288(21):15326–15341.
49. Lee KA, Nawrot M, Garwin GG, Saari JC, Hurley JB. Relationships among visual cycle retinoids, rhodopsin phosphorylation, and phototransduction in mouse eyes during light and dark adaptation. *Biochemistry*. 2010;49(11):2454–2463.
50. Kim GH, Kim HI, Paik SS, Jung SW, Kang S, Kim IB. Functional and morphological evaluation of blue light-emitting diode-induced retinal degeneration in mice. *Graefes Arch Clin Exp Ophthalmol*. 2016;254(4):705–716.
51. Bringmann A, et al. Cellular signaling and factors involved in Müller cell gliosis: neuroprotective and detrimental effects. *Prog Retin Eye Res*. 2009;28(6):423–451.
52. Izawa H, et al. Protective effects of antiplacental growth factor antibody against light-induced retinal damage in mice. *Invest Ophthalmol Vis Sci*. 2015;56(11):6914–6924.
53. Burns SA, Tumbar R, Elsner AE, Ferguson D, Hammer DX. Large-field-of-view, modular, stabilized, adaptive-optics-based scanning laser ophthalmoscope. *J Opt Soc Am A Opt Image Sci Vis*. 2007;24(5):1313–1326.
54. Zhang J, Yang Q, Saito K, Nozato K, Williams DR, Rossi EA. An adaptive optics imaging system designed for clinical use. *Biomed Opt Express*. 2015;6(6):2120–2137.
55. de Boer JF, Leitgeb R, Wojtkowski M. Twenty-five years of optical coherence tomography: the paradigm shift in sensitivity and speed provided by Fourier domain OCT [Invited]. *Biomed Opt Express*. 2017;8(7):3248–3280.
56. Huber R, Wojtkowski M, Fujimoto JG. Fourier domain mode locking (FDML): A new laser operating regime and applications for optical coherence tomography. *Opt Express*. 2006;14(8):3225–3237.
57. Kolb JP, Klein T, Kufner CL, Wieser W, Neubauer AS, Huber R. Ultra-widefield retinal MHz-OCT imaging with up to 100 degrees viewing angle. *Biomed Opt Express*. 2015;6(5):1534–1552.
58. Sawides L, et al. Alterations to the foveal cone mosaic of diabetic patients. *Invest Ophthalmol Vis Sci*. 2017;58(9):3395–3403.
59. Busskamp V, et al. Genetic reactivation of cone photoreceptors restores visual responses in retinitis pigmentosa. *Science*. 2010;329(5990):413–417.
60. Homma K, et al. Developing rods transplanted into the degenerating retina of Crx-knockout mice exhibit neural activity similar to native photoreceptors. *Stem Cells*. 2013;31(6):1149–1159.
61. Ovando-Roche P, Georgiadis A, Smith AJ, Pearson RA, Ali RR. Harnessing the potential of human pluripotent stem cells and gene editing for the treatment of retinal degeneration. *Curr Stem Cell Rep*. 2017;3(2):112–123.
62. Palczewska G, et al. Receptor MER tyrosine kinase proto-oncogene (MERTK) is not required for transfer of bis-retinoids to the retinal pigmented epithelium. *J Biol Chem*. 2016;291(52):26937–26949.
63. Duncker T, et al. Quantitative fundus autofluorescence and optical coherence tomography in ABCA4 carriers. *Invest Ophthalmol Vis Sci*. 2015;56(12):7274–7285.
64. Squier J, Muller M. High resolution nonlinear microscopy: A review of sources and methods for achieving optimal imaging. *Rev Sci Instrum*. 2001;72(7):2855–2867.
65. Bhardwaj V, Rajeshbhai GP. Axial length, anterior chamber depth-a study in different age groups and refractive errors. *J Clin Diagn Res*. 2013;7(10):2211–2212.
66. Coello Y, Xu B, Miller TL, Lozovoy VV, Dantus M. Group-velocity dispersion measurements of water, seawater, and ocular components using multiphoton intrapulse interference phase scan. *Appl Opt*. 2007;46(35):8394–8401.
67. Coello Y, et al. Interference without an interferometer: a different approach to measuring, compressing, and shaping ultrashort laser pulses. *J Opt Soc Am B*. 2008;25(6):A140–AA50.
68. Feeks JA, Hunter JJ. Adaptive optics two-photon excited fluorescence lifetime imaging ophthalmoscopy of exogenous fluorophores in mice. *Biomed Opt Express*. 2017;8(5):2483–2495.
69. Dysli C, Wolf S, Berezin MY, Sauer L, Hammer M, Zinkernagel MS. Fluorescence lifetime imaging ophthalmoscopy. *Prog Retin Eye Res*. 2017;60:120–143.
70. Ramaswamy M, Ulman M, Paye J, Fujimoto JG. Cavity-dumped femtosecond Kerr-lens mode-locked Ti:A1(2)O(3)laser. *Opt Lett*. 1993;18(21):1822–1824.
71. Theer P, Denk W. On the fundamental imaging-depth limit in two-photon microscopy. *J Opt Soc Am A Opt Image Sci Vis*. 2006;23(12):3139–3149.
72. Delori FC, Webb RH, Sliney DH, American National Standards Institute. Maximum permissible exposures for ocular safety (ANSI 2000), with emphasis on ophthalmic devices. *J Opt Soc Am A Opt Image Sci Vis*. 2007;24(5):1250–1265.
73. Chang CY, et al. Wavefront sensorless adaptive optics temporal focusing-based multiphoton microscopy. *Biomed Opt Express*. 2014;5(6):1768–1777.
74. Karpf S, Eibl M, Sauer B, Reinholz F, Hüttmann G, Huber R. Two-photon microscopy using fiber-based nanosecond excitation. *Biomed Opt Express*. 2016;7(7):2432–2440.
75. Murashova GA, et al. Multimodal nonlinear optical imaging of unstained retinas in the epi-direction with a sub-40 fs Yb-fiber laser. *Biomed Opt Express*. 2017;8(11):5228–5242.
76. Schwarz C, et al. Safety assessment in macaques of light exposures for functional two-photon ophthalmoscopy in humans. *Biomed Opt Express*. 2016;7(12):5148–5169.
77. Stremplewski P, Komar K, Palczewski K, Wojtkowski M, Palczewska G. Periscope for noninvasive two-photon imaging of murine retina in vivo. *Biomed Opt Express*. 2015;6(9):3352–3361.

78. Polynkin P, Kolesik M. Critical power for self-focusing in the case of ultrashort laser pulses. *Phys Rev A*. 2013;87:053829.
79. Fibich G, Gaeta AL. Critical power for self-focusing in bulk media and in hollow waveguides. *Opt Lett*. 2000;25(5):335–337.
80. Chen Y, et al. Mechanism of all-trans-retinal toxicity with implications for stargardt disease and age-related macular degeneration. *J Biol Chem*. 2012;287(7):5059–5069.
81. Maeda A, Maeda T, Golczak M, Palczewski K. Retinopathy in mice induced by disrupted all-trans-retinal clearance. *J Biol Chem*. 2008;283(39):26684–26693.
82. Chan F, Bradley A, Wensel TG, Wilson JH. Knock-in human rhodopsin-GFP fusions as mouse models for human disease and targets for gene therapy. *Proc Natl Acad Sci USA*. 2004;101(24):9109–9114.
83. Geng Y, et al. Optical properties of the mouse eye. *Biomed Opt Express*. 2011;2(4):717–738.